IGC Newsletter

IN THIS ISSUE

From the Editor

Dear Reader

It is my pleasant privilege to forward a copy of the latest issue of IGC Newsletter (Volume 112, April 2017 issue).

In the first technical article Shri K.V. Suresh Kumar and colleagues have shared their experience about the detection, identification of leak in FBTR steam generator module and replacement of the failed steam generator module.

In the second technical article Ms. T. Jayanthi and colleagues have shared about the Design and Development of VIKRAM Processor Based Remote Terminal Units for Fast Breeder Reactors.

This issue's young officer's forum features an article by Dr. A. Edward Prabu on Magneto-Transport Characteristics of Two-Dimensional States in 3D-Topological Insulators.
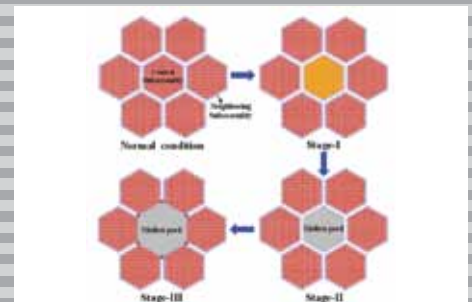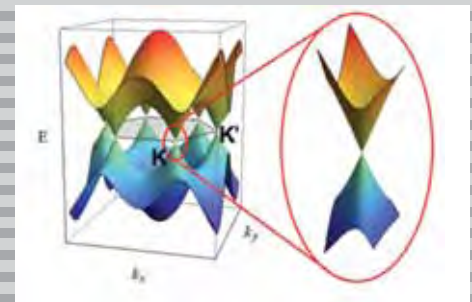
Dr. L. Ravi has discussed on Development of Thermal Hydraulic Model and Investigation of Core Damage Propagation during Total Instantaneous Blockage in SFR Fuel Subassembly in Young Researcher's Forum.

We had distinguished visitors to our Centre in the last quarter including, Dr. Y. V. N. Krishna Murthy, Distinguished Scientist, ISRO & Director, National Remote Sensing Centre, Hyderabad, Dr. Knut W. Urban, Ernst Ruska Centre for Microscopy and Spectroscopy with Electrons Research Centre Juelich, and Dr. Srikumar Banerjee, Homi Bhabha Chair Professor, DAE & Former Chairman, AEC.

We are happy to share with you the awards, honours and distinctions earned by our colleagues.

We look forward to your comments, continued guidance and support.

With my best wishes and personal regards,

Yours sincerely,

(M. Sai Baba)

Chairman, Editorial Committee, IGC Newsletter

& Director, Resources Management Group

Leak in the FBTR Steam Generator: Detection, Identification and Replacement of the Failed Steam Generator Module

Steam generator (SG) of FBTR is a once-through shell and tube type counter flow heat exchanger. The sodium flows in the shell side and water/steam through the tube side. There are two steam generator (SG) modules each in east and west secondary sodium loops connected in parallel. Each module rated for 12.5 MWt consists of 8 mm thick shell of outer diameter 198 mm and seven numbers 4 mm thick tubes of diameter 33.7 mm. The total heat transfer length is 90.4 metre and the material of construction is 2.25Cr-1Mo-Nb stabilized ferritic steel. The steam generator generates superheated steam at 125 kg/cm^2 and 480 ^{0}C by transferring nuclear heat from primary sodium to the tertiary steam water system through secondary sodium with inlet sodium at 510 ^{0}C.

As the sodium water reaction is exothermic with evolution of H$_2$, highly sensitive instrumentation (Figure 1) has been provided to detect incipient leaks from the tubes to sodium side. The leaks are categorized as small leak, medium leak and large leak. Small leaks are detected by sputter ion pump (SIP) based instrumentation system and safety action taken on crossing the absolute threshold and rate of increase of H$_2$ concentration in sodium. For this, three sputter ion pumps are provided in each loop which initiates safety action with a 2/3 logic. Medium leak is detected by increase in pressure of the expansion tank and large leak by bursting of rupture discs provided at the inlet and outlet of steam generator headers. Safety action is initiated by the signals from these systems. In addition to these, electrochemical hydrogen meter and hydrogen in argon detection by thermal conductivity detectors (TCD) are also provided, which give indication about increase in H$_2$ concentration in sodium and argon cover gas respectively.

On 7th October 2016, during 25th irradiation campaign at 27.3 MWt power, reactor tripped on leak at the western steam generator. The triplicated highly sensitive sputter ion pump based steam generator leak detection system (SGLDS) detected the tube leak. Signals
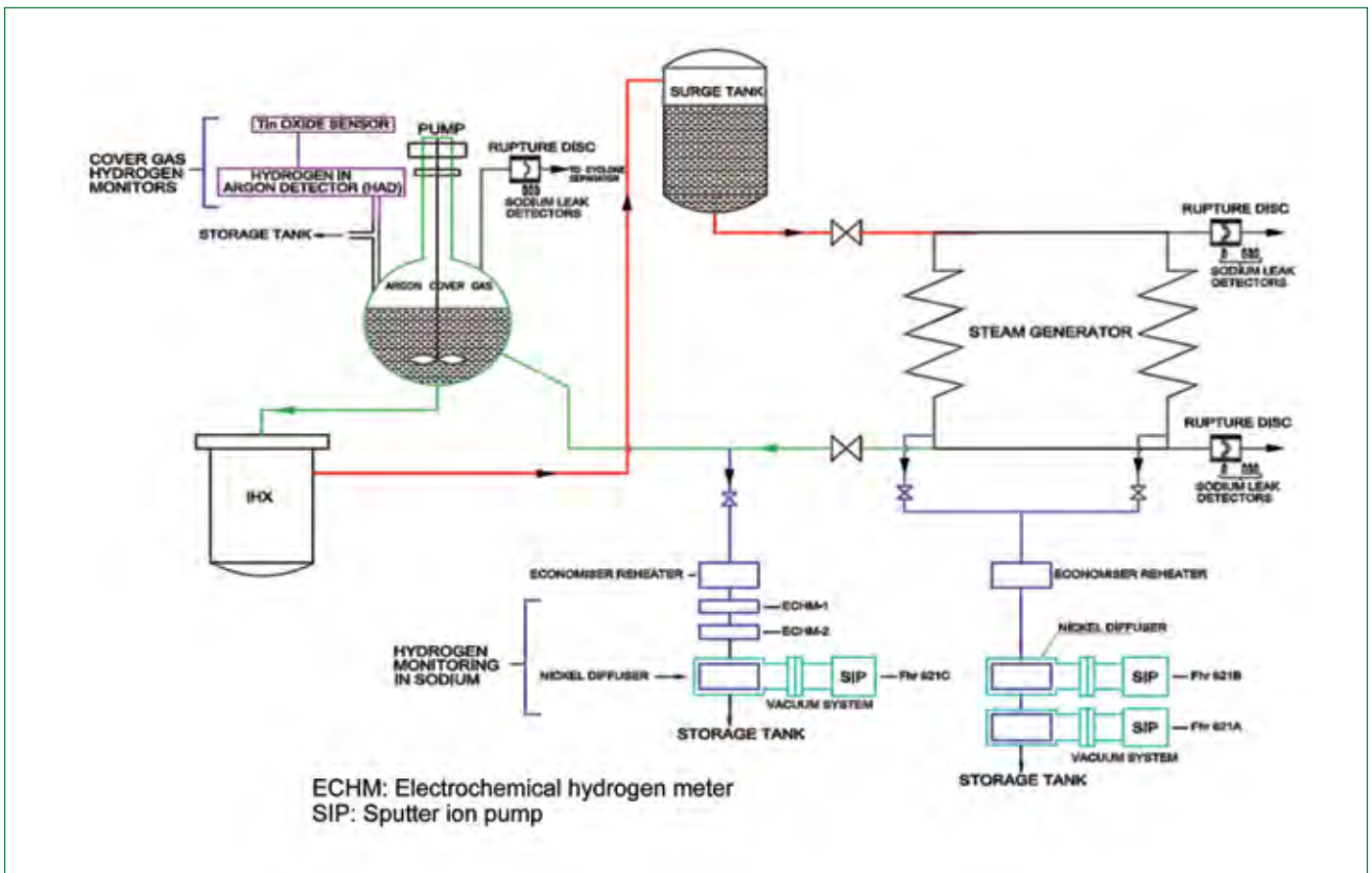

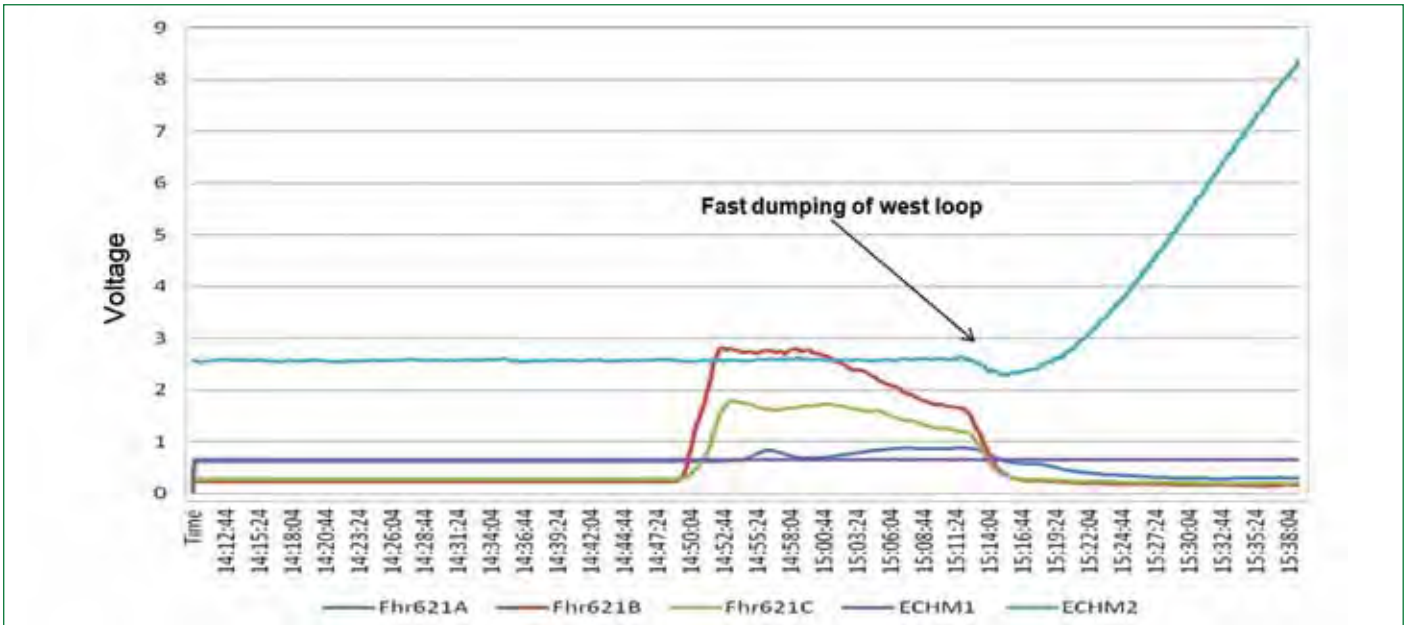Figure 1: Steam generator water/steam leak monitoring system

Figure 2: Response (voltage output) of sputter ion pump channels and electrochemical hydrogen meter(ECHM) channels

(Figure 2) from two detectors crossed the threshold initiating safety action automatically. After reactor trip, the steam generator modules in the affected west loop was put on "Safe Configuration" by isolating them from steam/water side, depressurizing the same and injecting nitrogen to the tube side to keep it inerted. Sodium from the loop was drained out subsequently.

Analysis of the cover gas in the expansion tank showed the concentration of H_2 as 5% and the plugging temperature of dumped sodium in the west loop was found to be 112 ^{o}C, as against the normal value of <105 ^{o}C. As any increase in hydrazine content in feed water and any oil leak from sodium pump also could cause

increase in H_2 concentration, the content of hydrazine in the feed water was measured and found to be normal and the level of pump oil was found to be steady. From these observations, it has been concluded that there is a genuine water/steam leak from one of the west loop steam generator modules into sodium. Conservative estimates based on the H_2 accumulation and the sodium plugging temperature in the west loop has indicated that the magnitude of leak is about 0.9 g/s.

As the two steam generator modules (SGna600A & SGna600B) remain interconnected at sodium side and steam/water side in the loop and there are no isolation valves, identification of the leaky

Figure 3: Steam generator module installation

Figure 4: Joint fit up and welding with system headers

module has become a big challenge. This was compounded by the fact that the quantum of leak was very minor, which occurred at high pressure (125 bar) and temperature (460 °C) and also that these conditions could not be recreated again for identifying the leak. Hence, a novel gas tracing technique was employed to identify the leaky module. Helium and argon gases at 40 bar pressure were admitted into SGna600A and SGna600B respectively. The shell side of the modules was sampled for the presence of helium. As no helium could be detected, the gases in the two modules were reversed. With helium in SGna600B and argon in SGna600A, presence of helium was detected in the shell side of SGna600B. At the end of six hours, helium concentration was found to be 1042 ppm indicating that SGna600B is leaking and the order of leak being very minute.

The failure of steam generator has been a first-of-the kind experience for FBTR and the replacement of the leaky module called for elaborate activities viz. cutting of water/steam/sodium headers, sodium cleaning/safe disposal and facilitation of operations including maintaining the system in inert atmosphere during the interventions, erection of massive scaffoldings inside and outside the steam generator casing, handling of structures like carrying beam, removal of hot beams, supporting steam generator modules to facilitate removal of the common support beams, modification of spare steam generator module to introduce welded orifice assemblies, requalification of the preserved spare steam generator module by helium leak testing of shell welds and tube side, removal of leaky module from the steam generator casing, introduction of spare module including positioning and alignment with common water header, steam header and sodium inlet/outlet headers, welding the joints, post-weld heat treatment of weld joints and qualification by liquid penetrant inspection, radiography, helium leak testing and finally by hydro testing of the tube side.

As FBTR is under the regulatory control of AERB, the incident, its consequences and the restoration plans were notified to AERB and approval has been obtained. The requalification of the spare module fabricated more than thirty years ago was completed.

A special task force including personnel from operations, maintenance, technical, quality assurance and industrial safety sections was constituted to execute the task. The task force made elaborate and meticulous planning, split major activities into smaller segments, entrusted each of them with small groups, integrated the split activities, did mock up of all major activities, qualified the crane for handling stresses by load tests.

The most difficult part of the entire programme has been the handling of the slender steam generator module of 200 mm diameter with overall dimensions (15 metre (L) x 6 metre (H)) and a weight of six tonnes inside steam generator casing, with narrow working space and absence of access by crane. Lifting of the module and movement of the module has to be done manually with utmost care and precision. The removal of the leaky module and the introduction of spare module were done by moving very slowly (inch by inch) and each operation lasted for about 8 to 9 hours.

Highest industrial safety standards were followed during the execution of work which spanned over more than 10 weeks and there was no accident or man-hour loss. Timely help from other agencies like Madras Regional Purchase Unit and Quality Assurance Division has expedited the schedule. The entire procedure could be completed in a record time of two and a half months against the original plan of four months. The systems were normalized and after observing the operating parameters of the steam generator, the reactor was raised to the target power of 27.3 MWt.

Reported by
K. V. Suresh Kumar and Colleagues
Reactor Facilities Group

Design and Development of VIKRAM Processor based Remote Terminal Units for Fast Breeder Reactors

Computer based embedded systems are developed for carrying out safety functions of the Fast Breeder Reactor. Distributed digital control system architecture is being followed for the plant monitoring and control of PFBR. The design philosophy of remote terminal units (RTU) is based on single board computer architecture. These RTUs are placed in Local Control Centre and geographically distributed across various buildings in the plant. It is our effort towards indigenization of components used in I&C systems, utilizing the expertise available in various other Government departments. Recently, Vikram Processor was handed over to IGCAR by VSSC, Trivandrum for its evaluation and making new system prototypes for various reactor applications.

Distributed Digital Control System

Distributed digital control system (DDCS) is the design architecture for automating a geographically distributed plant signals with large number of input/output signals and control loops. It facilitates in locating the data acquisition and control systems as close to the sensors and final control elements as possible, thereby saving lot of cabling and the associated electromagnetic interference problems. De-centralization also helps in modular development of the subsystems and in maintenance. The major constituents of DDCS are the sub-systems like VME bus based real time computer systems, standalone remote terminal units (RTU), electrical PLC system, process computer, display stations and the entire networking of systems. The architecture of DDCS is shown in Figure 1.

Remote Terminal Unit for FBR

RTU boards are designed for PFBR using 8051 Microcontrollers for remote data acquisition and control for acquiring analog/digital signals, sending/receiving digitized data packets over Ethernet using TCP/IP protocol and generating control outputs (digital/analog) during all states of plant operation. Field signals like analog input, thermocouples, leak detectors and digital inputs are received from various sensors from the plant. Control outputs are generated in the form of potential free contacts and current output to final control elements. These RTU boards are designed to work under field environment so as to reduce field wiring from sensors to local control centers (LCC) and to improve signal-to-noise ratio under harsh environments. RTU boards send digitized data to process computer, local display stations kept in LCCs and safety class display stations through respective data highways over Ethernet using TCP/IP protocol.

Vikram Processor Based RTU Board

Vikram 1601 is an indigenous designed microprocessor by VSSC, Trivandrum for acquisition of stage parameters of launch vehicles, processing and issuing of commands based on the inputs. Vikram processor is shown in Figure 2. It is a 16 bit RISC architecture

Figure 1: Architecture of distributed digital control systems

which supports external clock speed up to 80 MHz. The instruction set has 96 instructions including those for floating point arithmetic. This processor supports two addressing modes. In-circuit programmability and complex sequencing are also possible. Error handling is made simpler by tight synchronization with On-Board Computer (OBC). The processor finds application in realization of onboard computers for navigation, guidance and control processing in flight applications as well as for general purpose processing. As this processor has its own unique instruction set, all software development tools like Vikram Ada Compiler (VAC), Vikram Assembler (VASM), Vikram Linker (VLINK), Vikram System Generator (VSYS), Vikram Simulator (VSIM), Real Time Executive (REX) and all the library routines are developed in-house by VSSC, Trivandrum.

The chip is fabricated using CMOS fabrication facility at SCL, Chandigarh, which makes this particular processor fully
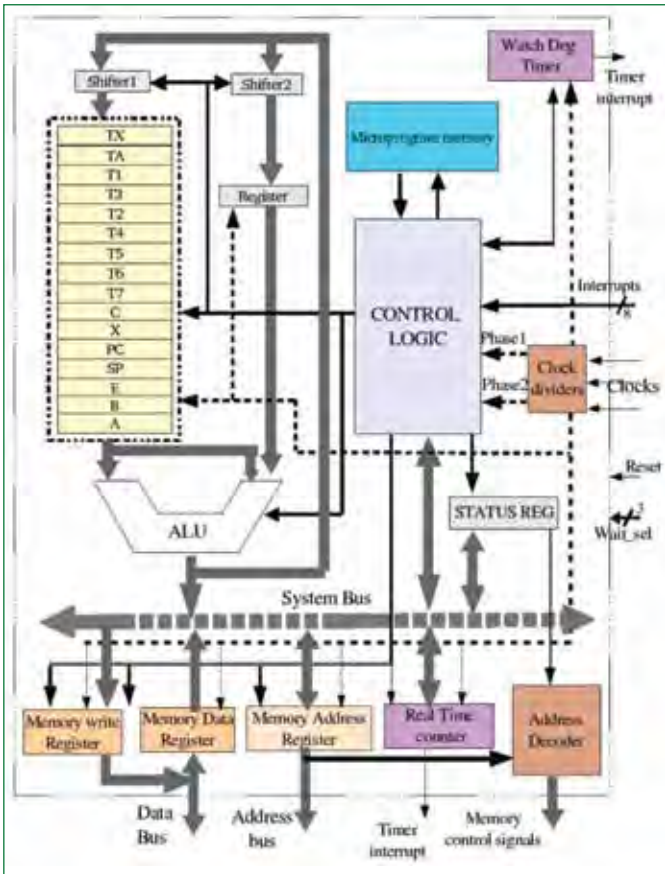

Figure 2: Vikram 1601 processor

Figure 3: Functional block diagram of Vikram 1601 processor

indigenous. The technology node used is 180 nm which is well proven and reliable. The functional block diagram of VIKRAM 1601 microprocessor is shown in Figure 3.

The major challenges posed to current I&C designers for fast reactors are that of component obsolescence and security. The adoption of Vikram 1601 processor will address both the issues as mentioned above. As it is developed indigenously, the design is available with the parent organization and hence can always be re-fabricated based on demand. The device manufacturing is done indigenously thereby leaving no scope for bug intrusion like Trojans during fabrication. The software tool chain uses ADA as the primary language for programming the microprocessor. ADA is a language intended for use in safety critical applications which suits to our

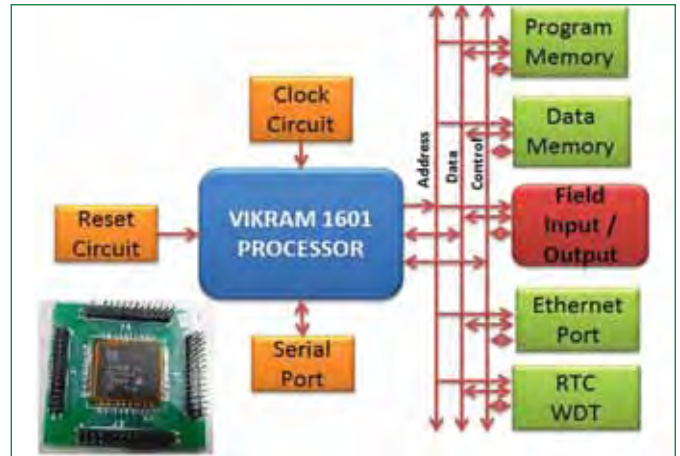Figure 4: Microcontroller based RTU board

Figure 5: Block diagram of Vikram 1601 processor based RTU board

requirements for developing SC-1, SC-2 and NNS systems for future FBRs. Additionally, the adoption of indigenously developed technology makes the system resilient against technology denial regime of foreign countries which has plagued Fast Breeder I&C community in the past. In the existing design of RTU board, Atmel make microcontroller is used as shown in Figure 4.

In our effort towards "Make-in-India", it is proposed to develop RTU boards by replacing Atmel make microcontroller with indigenously developed Vikram Processors for various applications in future FBRs like sodium leak detection, surface temperature measurements of sodium pipelines, fire protection, telealarm system, service water and chilled water system etc. The block diagram of proposed RTU board is shown in Figure 5. The peripheral components of Vikram processor such as program memory, data memory, serial port, dual ethernet port, clock, reset, real time clock, watch dog timer and I/O circuitry are connected through local address, data and control bus.

In order to cater various field requirements, it is proposed to design 16 channel analog input board to receive 0-10V/4-20mA signal; 16 channel thermocouple input board to receive K-type thermocouple signal with cold-junction compensation, open thermocouple detection and amplification; 16 channel leak detector board to receive signals from SPLD and WTLD sensors; 16 channel digital output board with opto-isolation and 4 channel analog output board during the prototype stage. The interface/glue logic between the processor and its peripheral components is envisaged to be implemented through a programmable logic device which would reduce the number of external components thereby increasing reliability and reducing the size of the board. The proposed boards will be subjected to the stringent design and qualification measures commensurate with the requirements for deployment in reactor environment.

Reported by
M. Sakthivel and colleagues
Electronics & Instrumentation Group

Young Officer's FORUM

Magneto-Transport Characteristics of Two-Dimensional States in 3D-Topological Insulators

Dr. A. Edward Prabu is working as a Scientific Officer at Low Temperature Studies Section (LTSS) of Materials Science Group (MSG). He joined the institute in 2013 from the 22nd batch of KSKRA. He obtained his M.Sc in physics from the University of Stuttgart, Germany and his Ph.D. from Max-Planck Institute for Intelligent Systems, Germany (formerly Max-Planck Institute for Metals Research). His current area of interest comprises magneto-transport properties of topological insulators, magnetic materials, superconductors and novel two-dimensional (2D) materials for sensor applications.

Graphene, a single sheet of sp^2 bonded carbon atoms, is believed to be the building blocks of next generation sensors and electronics devices. Due to its two-dimensional (2D) nature, they exhibit linearly dispersed electronic bands called Dirac cones (DC) as shown in the Figure 1a. Their exceptional properties such as high electron mobility, high current density, and high thermal conductivity are due to the presence of these Dirac cones states in these systems. However, the lack of band gap in graphene hinders it to be compatible with the semi conducting devices, and therefore it has triggered the search for another alternate 2D semiconducting materials. Boron nitride and more recently, mono-elemental class of 2D crystals such silicene, germanene, stanene, generally termed as 2D-Xenes (X=Si, Ge, Sn) have attracted immense research interest. Transition metal dichalcogenides (TMDs) are also atomically thin semiconductors of the type MX_2, where a transition metal atom (M = Mo, W etc.) is sandwiched between chalcogen atoms (X = S, Se, Te). All these 2D materials are more promising for fundamental research, as well as for advanced and entirely novel technologies. However, large scale isolation of the 2D atomic monolayer for mass production of devices is still challenging.
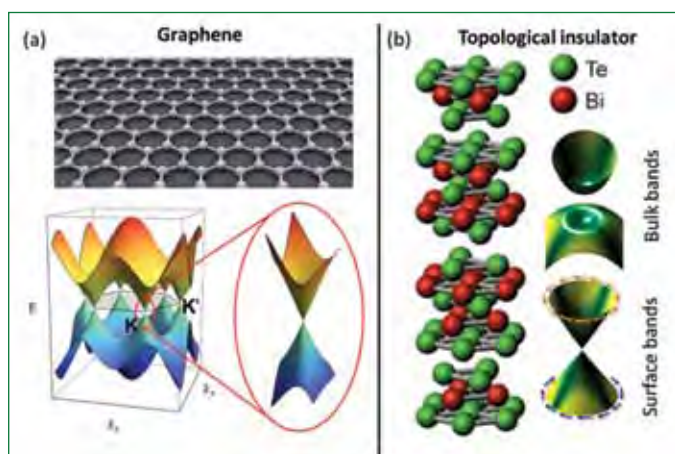

Figure 1: (a) Schematic representation of a single atomic layer of sp^2 carbon atoms in graphene and Dirac cone states with linear dispersion and (b) shows the layered arrangement of atoms in TI and Dirac cones existing within the bulk band gap (adapted from literature)

Bismuth-based chalcogenides such as Bi_2Se_3, Bi_2Te_3, and their derivative have been extensively studied over the past five decades for their thermoelectric properties. The recent spurt of the renewed intense research on these materials has arisen after they were theoretically proposed and experimentally confirmed to be a new class of materials called Topological insulators (TI). Similar to graphene, these layered materials also possess linear 2D electronic states within the 3D bulk states as shown in the Figure 1b. However, in contrast to graphene, these 2D states in TI are due to the strong spin-orbit coupling in the bulk crystal. Interestingly, these 2D states are spin polarized, less susceptible to localization, back scattering and are more favorable for application in spintronics and quantum computing.

In magneto-transport measurements, oscillation in resistance with a magnetic field (Shubnikov-de Haas oscillations (SdH)) and positive MR with sharp cusp known as weak anti localization (WAL) are fingerprints of these surface states (SS).The 2D surface contribution is often masked by undesirable excess charge carriers arising on account of the unintentional defects, impurities, antisite disorders and vacancies states in the bulk. Significant efforts have been made to suppress these metallic contributions by adopting different preparation methods, doping or by growing thin films to increase the surface to bulk ratio. However, the effect of intrinsic and induced defects in TI and their influence on the surface states are less studied. Here we study the magneto transport properties of Bi_2SeTe_2 (BTS) topological insulator grown with quenched in disorders and the annealing-induced modification of electronics defects in the samples.

Experimental Details

Single crystals of BTS were prepared by melting the stoichiometry mixture of Bi, Se, and Te in an evacuated quartz crystal at 850˚C for six hours. The melt was cooled at a faster cooling rate
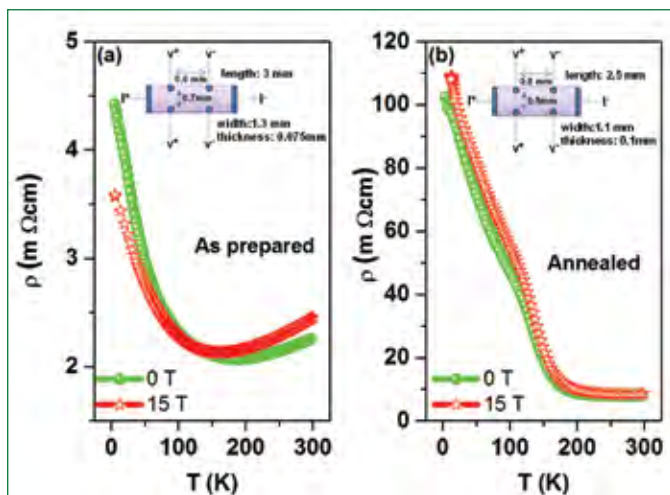
Figure 2: Temperature dependence of resistivity at 0 and 15 T measured on (a) the pristine and (b) the annealed sample. Insets in (a) and (b) shows the sample and the contact dimensions

Figure 3: Magnetoresistance data of (a) pristine and (b) annealed sample measured in the magnetic field range of $\pm$ 15 T at 4 - 300 K

($\sim 137^{\circ}$ C per hour) to induce electronic disorders in the sample. Few crystals were post-annealed in vacuum at 500°C for 6 hours and cooled back to room temperature at the rate of 50°C per hour. Temperature, magnetic field dependent resistivity studies and Hall measurements were carried out in Van der Pauw and six-probe geometry in a commercial, 15 T Cryogen-free system. Electrical contacts on a cleaved crystal were made using a 20 micron Au wires attached on the sample surface with silver paste curable at room temperature. The sample and contact dimensions are shown in the inset of Figure 2.

Temperature Dependence of Resistivity and Hall Measurements

Temperature and field dependent magneto resistance (MR) studies were performed on pristine and annealed BTS samples. Temperature dependent resistivity [ρ(T)] of the pristine sample presented in Figure 2a shows a metallic behavior from 300 down to 180 K and an upturn at T < 180. ρ(T) measured at 15 T also shows a similar trend but with a prominent crossover at 130 K. This crossover in R(T) indicates a change in the slope of MR from negative at low T to positive at high T which is discussed later. The post-annealed sample shows an increase in the overall resistivity value by one order of magnitude and the ρ(T) increases by two orders of magnitude with decreasing temperature (Figure 2b). At the zero magnetic field, the slope of the ρ(T) changes at 115, 65, and 20 K, whereas at B=15 T it changes only at 100 K while the overall trend of ρ(T) remains the same. It should be mentioned that there are no signatures of any crossover of R(T) as previously observed in the pristine sample.

To get further insight into the changes observed in ρ(T), MR [defined as ρ(B)- ρ(0)] measurements were carried out at different temperatures in the field r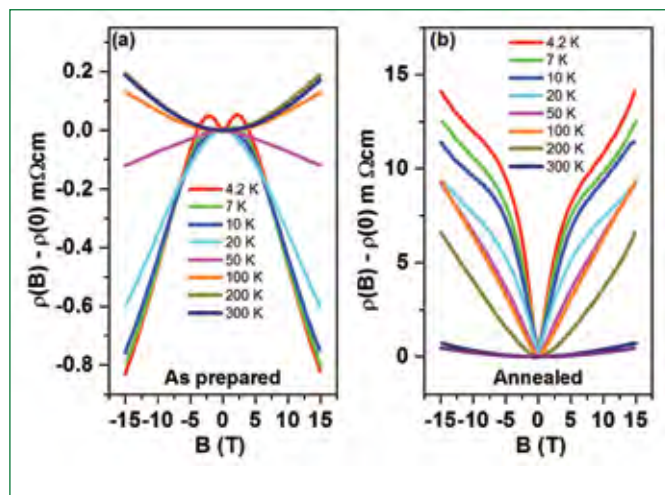ange of $\pm$ 15 T. Figure 3a shows field dependent MR behavior of the pristine sample at several fixed temperatures from 4.2 to 300 K. MR shows a clear positive cusp at 4.2 K for B < $\pm$2.5 T while for B > $\pm$2.5 T MR decreases with increasing field. The former feature is known as weak anti localization (WAL) and the later as weak localization (WL) effects due to the interference of the diffusing electron paths in the sample. The WAL feature and the magnitude of negative MR decrease as the temperature increases (7,10 K) and it gradually transforms to classical B^2 dependence at T$\geq$ 100 K. This crossover is also evident in ρ(T) in which the 0 T curve intersects the 15 T curve at $\sim$ 130 K (Figure 2a).

In contrast, the annealed sample does not exhibit any signature of WL (Figure 3b). For T < 20 K, it rather depicts a WAL cusp for B < $\pm$10 T and a parabolic behavior for the higher field (B > $\pm$10 T). The magnitude of the MR and the parabolic component decreases upon increasing the temperature upto 20 K. Interestingly, linear magnetoresistance (LMR) is observed at 40, 50 and 100 K. At 200 and 300 K, a classical B^2 dependence is retained similar to that of the pristine sample.

To understand the ρ(T) and ρ(B) behavior, Hall measurements were carried out to study the changes in carrier densities and its mobility. In Figures 4a and 4b both the pristine and the annealed samples show a non-linear behavior at 4.2 K, while a linear trend is observed at higher temperatures (T$\geq$10K). The non-linear Hall arises due to the parallel contribution of two types of carriers with different mobility. From Hall and resistivity measurements, the carrier density (n), mobility (ρ) and the Ioffe-Regel parameter ($k_F l$) were obtained. k_F the Fermi wave vector and l is the mean free path of the electron. The carrier density was calculated from the slope of the R_{xy} versus B plot at B >10 T.
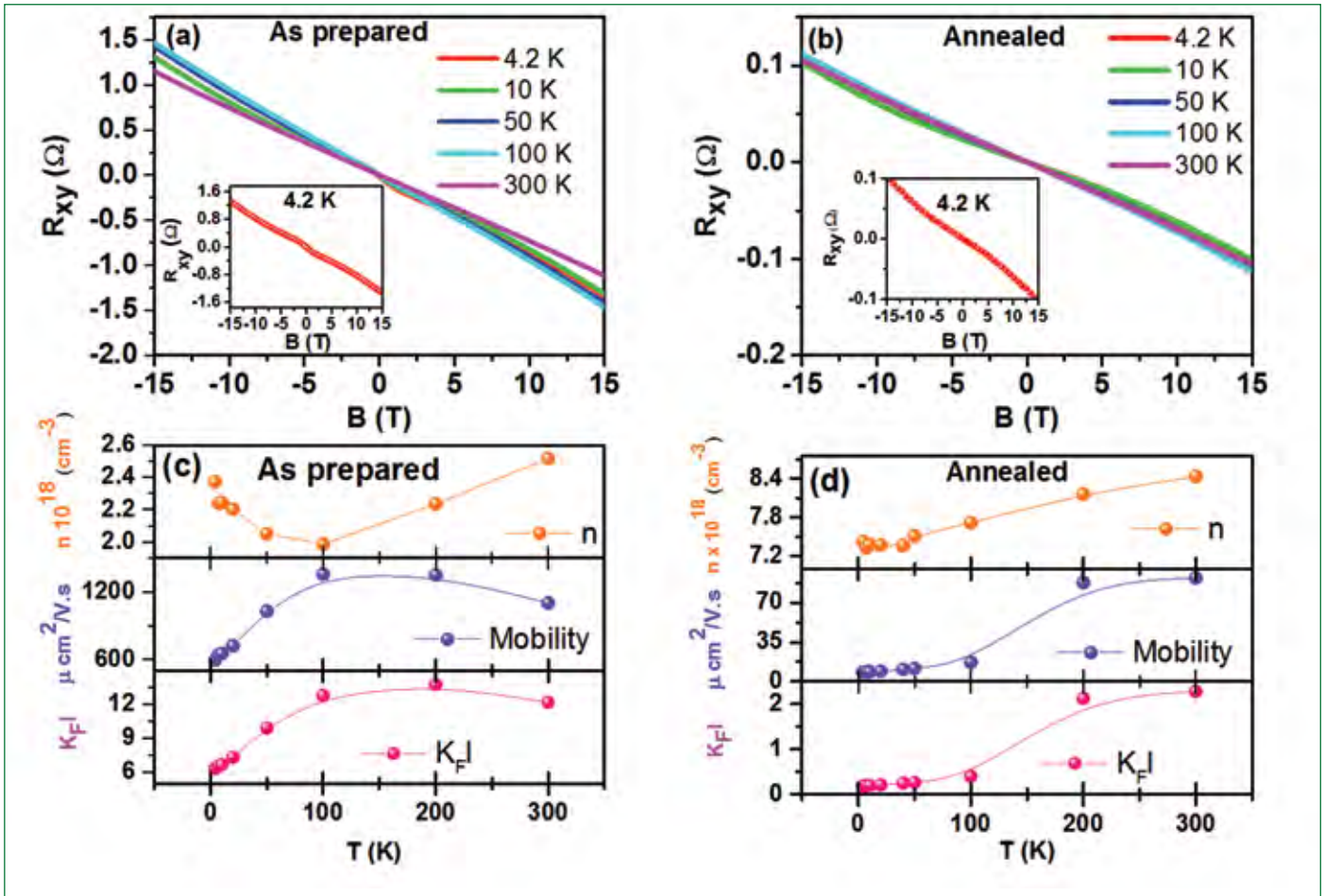
Figure 4: Hall data of (a) the pristine and (b) the annealed samples at various fixed temperatures. Insets in respective panels show the non-linear behavior observed at 4.2 K. (c) and (d) shows the temperature dependence of carrier density (n), mobility (μ), and $k_F l$ for pristine and annealed sample respectively

The insulating character of TI can be attained either by Mott criterion in which carriers are reduced or by Ioffe-Regel criterion in which the mobility is reduced due to electronic disorder in the sample. For good metals the Ioffe-Regel criterion $k_F l > 1$ and for bad metals $k_F l < 1$.

To clarify whether the carrier density or the mobility drives the sample to the insulating nature, the temperature dependence of n and ρ are shown in the Figures 4c and 4d. The carrier density increases by a factor of 3 upon annealing whereas the mobility decreases by one order of magnitude. It shows that annealing has increased the donor impurities, probably the selenium vacancies, and introduced more disorder in the lattice. Consequently, the Ioffe-regal parameter also decreases as compared to the pristine sample. The temperature evolution of these parameters shows a marked difference between the two samples. For a pristine sample, ρ and $k_F l$ increases marginally with decreasing temperature and shows a sharp decline on a further decrease in T. Whereas n decreases initially as the temperature decreases and for T < 100 K it shows an increasing trend (Figure 4c). In the case of the annealed sample, the values of n, ρ, and $k_F l$

decrease monotonically up to T∼100K with decreasing temperature and then exhibit a saturating trend for T < 100 K.

In the context of the transport properties of the pristine sample, it is seen that the essential features, about temperature and field dependence of the resistivity and the Hall data, can be rationalized based on the presence of disorder in this TI system which possesses bulk as well as surface charge carriers. The presence of disorders lead to the formation of a disordered potential forcing the bulk charge carriers to traverse through it. As the temperature decreases, the mobility of carriers reduces drastically (Figure 4c) compelling the system to tend at the verge of localization which gives rise to an upturn as seen in the ρ(T) at low T. On the other hand, the surface electrons, which are immune to localization and back scattering, contribute to the total conductivity in parallel with the bulk carriers.

The parallel contribution of both the surface and the bulk carriers can give rise to the WAL and the WL features as observed in our experiments. In the case of the annealed sample (Figure 3b), a remarkably different MR behavior is observed in three temperature

regimes: (i) WAL cusp for B < ±10 T and parabolic behaviour for B > ±10 T at T < 20 K, (ii) LMR at intermediate temperatures (40≤T≤100 K) and (iii) quadratic MR above 100 K. The absence of the WL, in contrast to that seen in the pristine sample, and the presence of the WAL in annealed samples could be due to the enhancement of disorder in the latter on account of the formation of stronger disorder potential leading to further localization of bulk carriers and thereby decreases the ratio of bulk to surface carriers.

The LMR can be either of quantum origin as derived by Abrikosov or of classical origin put forth by Parish-Littlewood model. Since the quantum LMR requires extreme condition at which the lowest Landau levels are occupied, it can be ruled out to explain our LMR. The classical model is caused by the mobility (ρ) fluctuating in the sample. Therefore the temperature evolution of the ρ should show a linear dependence with the slope of the LMR. In our experiments, the mobility changes by a factor of two whereas the slope of the LMR (dMR/dB) at 40, 50 and 100 K remains almost constant in the high field region. Therefore, the classical model can also be ruled out.

We have fitted our magneto conductivity (MC) with the modified Hikami-Larkin-Nagaoka (HLN) equation that describes the localization effect.

$$\sigma(B) - \sigma(0) = (N_{ch}e^2/\pi h)[\psi(0.5 + h/4el_\varphi^2 B) - \ln(h/4el_\varphi^2 B)] + \beta B^2 \quad \ldots \ldots \ldots (1)$$

Here Ψ is the digamma function, l_ϕ is the phase coherence length, B is the magnetic field, N_{ch} is the number of conducting channels. β is the quadratic coefficient which contains both quantum scattering term and the classical cyclotron term. Figure 5 shows the representative fit of magneto conductivity data of the annealed sample. It can be seen that Equation 1 fits very well for the magnetic field B < ± 10 T for temperatures below 50 K. At temperatures T≥10 K the HLN equation yields better fit in the entire field range. The deviation of the fits above 10 T, particularly in low T (T ≤ 10 K) shows that the condition for which the above-modified HLN equation holds is not fulfilled in the entire field and the temperature range.

The extracted phase coherence length from the fit and its temperature dependence are shown in the inset of Figure 5. It is noticed that the l_ϕ shows $l_\phi \sim T^{-p}$ type of power law decay with two different P values operating in two temperature ranges. For T < 20 K, it decays with exponent P ~ 0.28, while for T > 20 K the decay is found to be faster with P ~ 0.62. Though it is tough to attribute the decay constant P either to electron-electron interaction in 2D surface/3D bulk channels or electron-phonon interaction, it could be qualitatively inferred that these P values can be due to the different ratio of surface to the bulk carrier and temperature
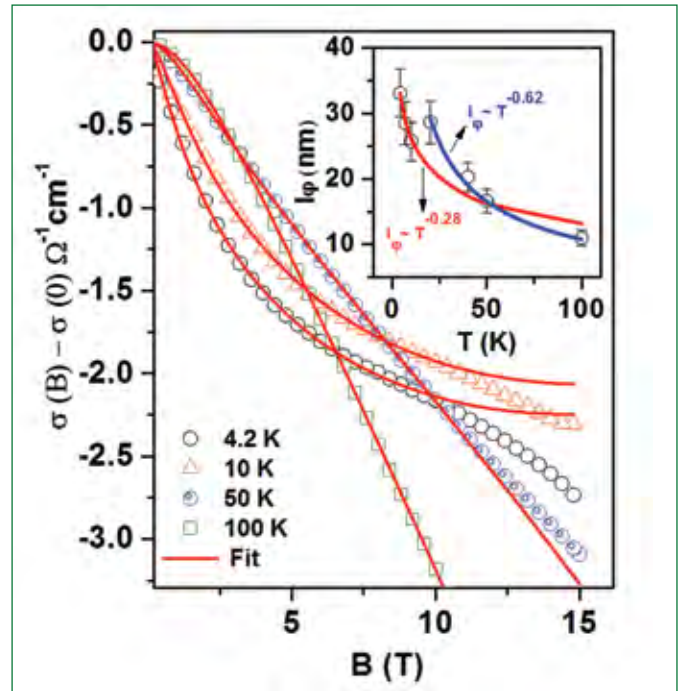

Figure 5: Magneto conductivity data of the annealed sample with its fit with modified HLN equation. The inset shows the temperature dependence of phase coherence length (l_ϕ) deduced from the fit with two distinct decays coefficient operating at different T

and magnetic field dependence of their interactions. It is interesting to mention that the crossover of P seen around T ~ 20 K also correlates with the crossover behavior seen in the MR around this temperature. MR exhibits a linear trend for T > 20 K whereas the WAL with the quadratic component is observed for T < 20 K (4, 7, 10 K).

We have shown that the nature of electronic transport in a disordered BTS TI single crystal drastically changes upon annealing. As-prepared sample shows WAL and WL behavior at low temperature whereas the annealed sample exhibits WAL with a parabolic component. At intermediate temperatures, the annealed sample showed an LMR behavior and the MR had been fitted with a modified HLN equation. The parallel conductance of surface and bulk channels is believed to cause the coexistence of the WAL and the WL in the pristine sample. The compensation of the quantum logarithmic term and the classical quadratic term is anticipated to cause the LMR in annealed sample. These studies show that tailoring the defects in TI samples can lead to the interesting linear variation of resistance with a magnetic field which will be useful for sensor applications. Tuning the TI system to exhibit LMR at accessible temperatures will be the future aspects of this research.

Reported by
A. Edward Prabu and Colleagues
Materials Science Group

Young Researcher's FORUM

Development of Thermal Hydraulic Model and Investigation of Core Damage Propagation during Total Instantaneous Blockage in SFR Fuel Subassembly

Dr. L. Ravi joined as a DGFS PhD Fellow at Nuclear Systems Analysis Group, Reactor Design Group. His research work is involved in thermal hydraulic investigation on radial propagation of damage to core subassembly due to total instantaneous blockage in a single fuel subassembly.

A local flow blockage in a fuel subassembly (SA) reduces the coolant flow to the subassembly causing a corresponding rise in the coolant temperature at subassembly outlet. Such blockages are expected to grow gradually and the core outlet coolant monitoring thermocouples located at the top of every subassembly are capable of detecting them at their infancy. But, large size blockages may not be detected by the thermocouple due to low velocity of sodium issuing from the blocked subassembly and the strong masking effect from the neighboring subassembly sodium streams. One of the initiating events for severe accident scenario in sodium cooled fast reactors is flow blockage in the subassembly. Traditionally, total instantaneous blockage (TIB) at the inlet of the subassembly when the reactor is operating at full power is considered as an enveloping event. During the initial stage of a total instantaneous blockage event, imbalance between the rate of heat generation by fuel pins and cooling capability leads to continuous rise in temperature of fuel, clad and sodium within the blocked subassembly. As a consequence of this, coolant boiling takes place, followed by clad and fuel melting. During these transient phenomena, there is inter-subassembly heat transfer from the blocked subassembly to neighboring subassembly. Monitoring the sodium outlet temperature of the neighboring subassembly and initiating safety actions once the measured thermocouple reading exceeds the specified threshold value is one of the means to detect the blockage in the subassembly.

During total instantaneous blockage in a single subassembly, the sequence of damages taking place within the blocked subassembly, viz., sodium boiling, followed by melting of clad, fuel and hexcan results in progressive change in the geometric configuration of the blocked subassembly. Further, a fuel pool is formed attacking the neighboring six subassemblies. These are complex thermal hydraulic phenomena involving moving solid-liquid interfaces, phase change heat transfer and natural convection in fuel pool. In European countries, US and Japan, capability to analyse this event

has been established by a joint development of the popular SIMMER code series. But, this code is not accessible to India. Hence, a 2-dimensional thermal hydraulic model has been developed as a part of the research. This model considers axial power distribution in the fuel pin and natural convection that sets within the fuel pool which enhances damage propagation.

Internationally, SCRABEE-N in-pile experimental test program was carried out to understand the consequences of total instantaneous blockage in sodium cooled fast reactor. This program was focused on the three stages of the total instantaneous blockage scenario, viz., (i) evolution of scenario inside the blocked subassembly, (ii) melt-through of blocked subassembly and damage progression to inter-subassembly gap and (iii) melt-through of the neighboring hexcan wall and propagation of damage to neighboring subassembly. The rapid failure of subassembly hexcan during core disruptive accidents was investigated by in-pile experiment under EAGLE project. The failure mechanism of stainless steel hexcan wall due to molten oxide attack during subassembly melt propagation accident in SFRs was experimentally investigated in the SCRABEE BE+3 in-pile test. This experiment suggested four different hexcan failure mechanisms. Theoretical studies related to total instantaneous blockage in fuel subassemblies of (i) French SPX-1 and PHENIX reactors using an in-house codes (details of which are not reported in open literature) and (ii) Chinese Experimental Fast Reactor (CEFR) and other Japanese reactors using SIMMER codes have been reported. The 3-D models adopted in SIMMER series of codes are very complex and highly demanding in computer time. Thus, there is a need to develop a transient 2-dimensional computational model, which has been largely accomplished as a part of this research.

Modelling Features

To predict the evolution of various key phenomena and to estimate the subsequent response of the neighboring subassembly thermocouple, a mathematical model has been developed by classifying the event progression in to three stages as depicted in Figure 1. The features of the calculation model for various stages are detailed below.

Stage-I

In stage-I, detailed thermal hydraulic analysis of various events inside the blocked subassembly before its hexcan gets damaged is carried out. A prototype hexagonal subassembly of 217 pins arranged in 8 rows is geometrically modeled by an equivalent 2-D axi-symmetric domain. The geometrical modeling represents central (blocked) subassembly, inter-wrapper sodium, and neighboring subassembly hexcan (Figure 2). Axial power distribution in the fuel pin is assumed to be a cosine profile. Initial calculations are carried out before conducting transient analysis to determine the steady state temperature distribution in fuel, clad, sodium and hexcan of central subassembly as well as the neighboring subassembly. Fuel pin power distribution, sodium inlet temperature and sodium mass flow rate required for steady state calculations are obtained from basic heat balance. The steady state temperature distributions are obtained by numerically solving the non-linear 2-D transient energy equations by time-marching. During the transient, various parts of the subassembly undergo temperature change as well as phase change. To model these complex phenomena, viz., sodium boiling, clad/hexcan melting, fuel melting etc., an enthalpy formulation is adopted. The features of the model include,

- (i) Enthalpy based energy equations for fuel, clad, hexcan and sodium
- (ii) Effective conductance between the nodal points
- (iii) Radiation heat exchange between the nodes, when sodium has completely boiled out
- (iv) Temperature-dependent physical properties
- (v) Delayed response of core monitoring thermocouples.

Stage-II

The clad melting and liquid steel draining down, during stage-1 result in formation of steel blockage at the bottom of active region. Further melting of fuel leads to accumulation of molten material over a steel blockage forming a molten fuel pool in the blocked subassembly and attacking its hexcan. It is also required to estimate the time taken for complete melting of blocked subassembly hexcan and corresponding inter-subassembly heat transfer. The effective height of the molten fuel pool formed is decided by the quantity of the fuel in the blocked subassembly. The heat transfer is predominant in radial direction to six sides of hexcan, which are externally cooled by inter-wrapper sodium flow. This configuration resembles to a heat generating fluid column in an externally cooled container. Thus, a large temperature difference develops in the fuel pool leading to natural convection which augments the radial heat transfer from the pool to the neighboring subassembly. Meanwhile molten pool damages the hexcan. The rate and extent of damage propagation depend strongly on the time dependent radial heat flux emerging during natural convection that takes place within the fuel pool. The flow and heat transfer during natural convection in the molten fuel
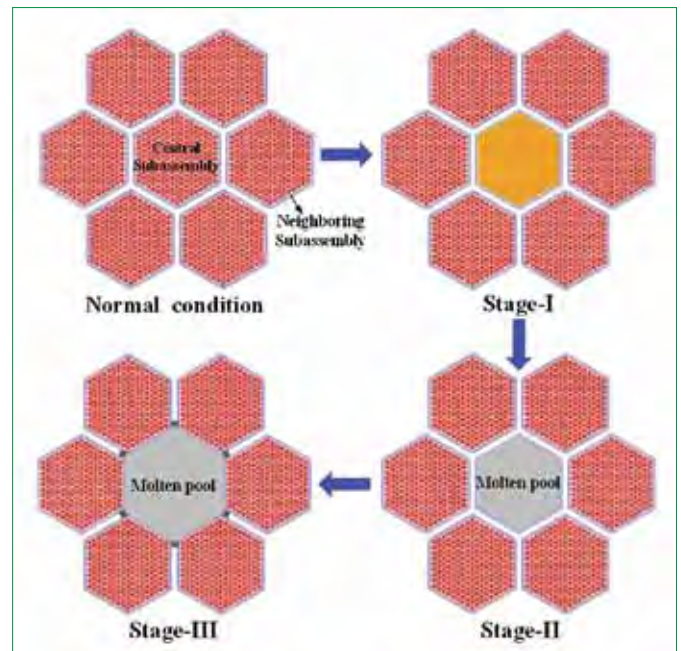

Figure 1: Sketch showing TIB event progression: Normal condition, stage-I: transients within blocked subassembly before hexcan failure, stage-II: molten fuel attacking blocked subassembly hexcan and stage-III: molten fuel attacking neighboring hexcan

pool are governed by the transient, mass, momentum and energy equations along with conservation equations for turbulent kinetic energy and turbulent dissipation rate, as in standard computational fluid dynamic (CFD) simulations. The solution to these equations is obtained by the finite volume method using the SIMPLE algorithm.

Stage-III

After the failure of blocked subassembly hexcan due to molten fuel attack during stage-II, the melt front advances radially towards the neighboring subassembly. The molten fuel attacks neighboring
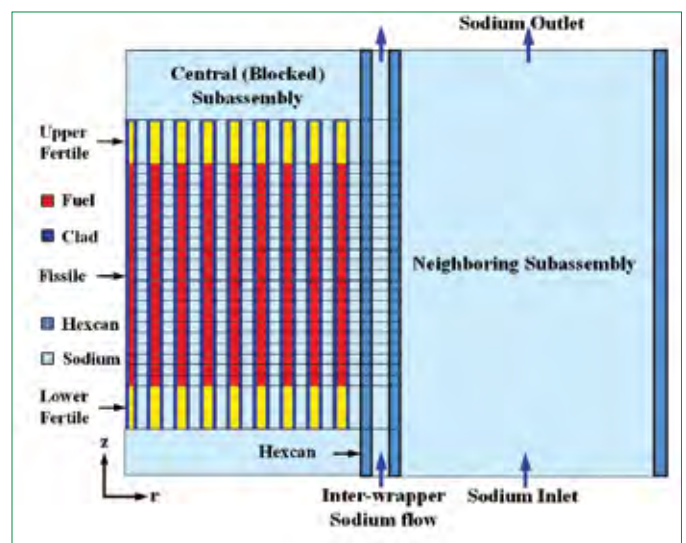

Figure 2: Geometrical model with mesh for central (blocked) subassembly with neighboring subassembly

Table 1: Instants of occurrence of various events during a TIB						
	Time (s)					
Process	**Numerical study**			**Experiment study**		
	PFBR (Present)	**Phenix**	**CEFR**	**SCARABEE-Test**		
				BE+1	**BE+2**	**BE+3**
Start of total instantaneous blockage	0	0	0	0	0	0
Start of sodium boiling	0.5	0.5	1	3	2	-
End of sodium boiling	4.0	5	2.5	-	3	-
Start of clad melting	4.3	6	2.5	6	5.5	-
End of clad melting	8.5	9.2	6	-	-	-
End of fuel melting	16	-	15	-	-	-
End of blocked hexcan melting	18	18.5	16.6	-	-	21

subassembly hexcan and starts melting them. Stage-III is focused to investigate thermal transients during melting of neighboring subassembly hexcan and to determine the rise in the neighboring subassembly sodium outlet temperature.

Validation

The computational model developed has been subjected to detailed validation by solving both academic and application related benchmark problems. The sequence and time of occurrence of principal events during total instantaneous blockage predicted by the model are presented in Table 1. Results of total instantaneous blockage analysis reported for prototype fuel subassemblies of CEFR and Phenix reactors are also presented in the same table. It is clear that the present results compare satisfactorily with the reported data, generated using advanced SIMMER code. The results of SCARABEE Test carried out on small subassemblies are also presented in Table 1. The predicted evolution of neighboring subassembly sodium outlet temperature from the present study

was compared with that reported for SPX-1 reactor and the present results were found to compare very well with reported data.

Results of Flow Blockage in Prototype Fuel Subassembly

Detailed investigation of total instantaneous blockage accident in a single subassembly of a 500 MWe SFR has been carried out. The fuel subassembly with 217 fuel pins has a thermal power of 8 MW at normal operation with sodium mass flow rate of 35.8 kg/s. Temperature of sodium at inlet and outlet of the subassembly are 400 and 560 °C respectively. Before initiating the actual transient calculations, the temperature distribution in fuel, clad, sodium and hexcan of central and neighboring subassembly operating at normal reactor operation condition are calculated, which form initial conditions for the transient analysis.

Stage-I

The predicted initial steady state temperature distribution in fuel, clad and sodium in the central region of the blocked subassembly are
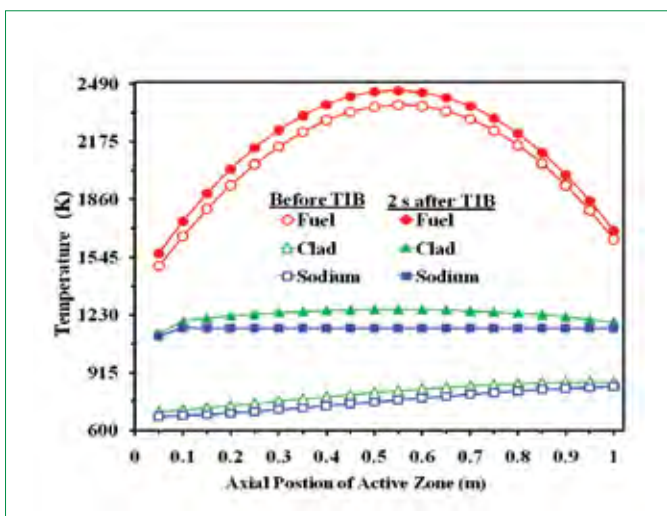

Figure 3: Temperature evolution of fuel, clad and sodium in the center region of the blocked SA within the active region, before TIB and two seconds after TIB
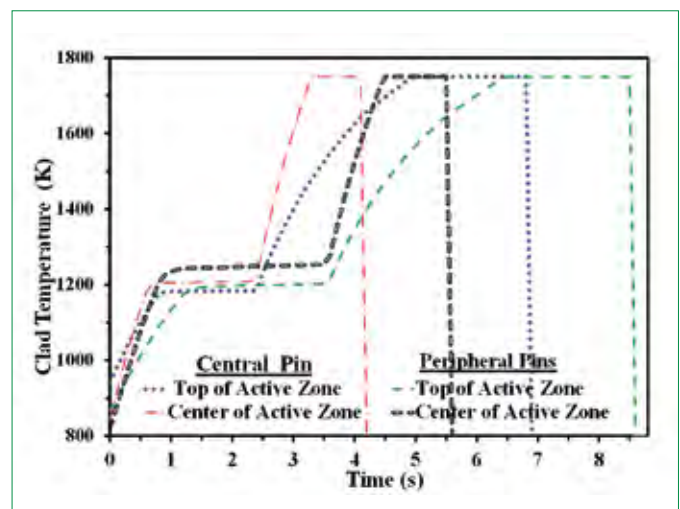

Figure 4: Evolution of clad temperature in the central and peripheral regions of the blocked SA during stage-I
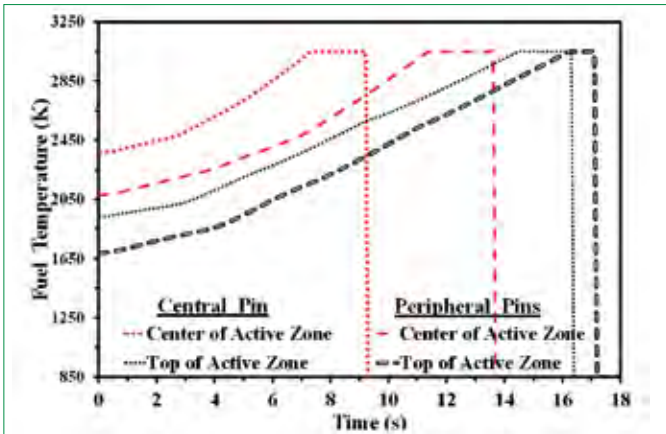
Figure 5: Temperature evolution of fuel pellet at central and peripheral rows during stage-I

depicted in Figure 3. There is a gradual increase in clad and sodium temperature along the vertical direction, while the fuel temperature follows the cosine profile true to the power distribution. Within 2 seconds after the total instantaneous blockage, the sodium starts boiling and the clad temperature also increases sharply and marginally exceeding the sodium boiling point.

The clad temperature closely follows the sodium temperature till entire sodium is vaporized. Accordingly, sodium boiling is first observed at ~0.5 seconds after total instantaneous blockage, in the central pin region at the top of the active zone (Figure 4). Further, boiling propagates rapidly in both axial and radial directions and reaches the peripheral region at about 0.8 seconds. Sodium voiding in the blocked subassembly starts at about 2 seconds in the central region of the subassembly (Figure 6b) and propagates rapidly inducing sodium dry-out at about 4 seconds. Sodium dry-out in the blocked subassembly is immediately followed by clad melting. Sodium vapor in the subassembly creates adiabatic environments around the cladding surface, causing sudden rise in clad temperature. Clad failure is first noticed in the central pin at the mid of the active height at about 4.2 seconds after total instantaneous blockage (Figures 4 and 6c). Further, clad at top of the active zone of the central pin completes melting at about 7 seconds after total instantaneous blockage. This delay is due to low local heat generation rate of the fuel element at the top of the active zone. It is learned from the SCARABEE-N experimental program that clad draining down after clad melting, settles at the bottom
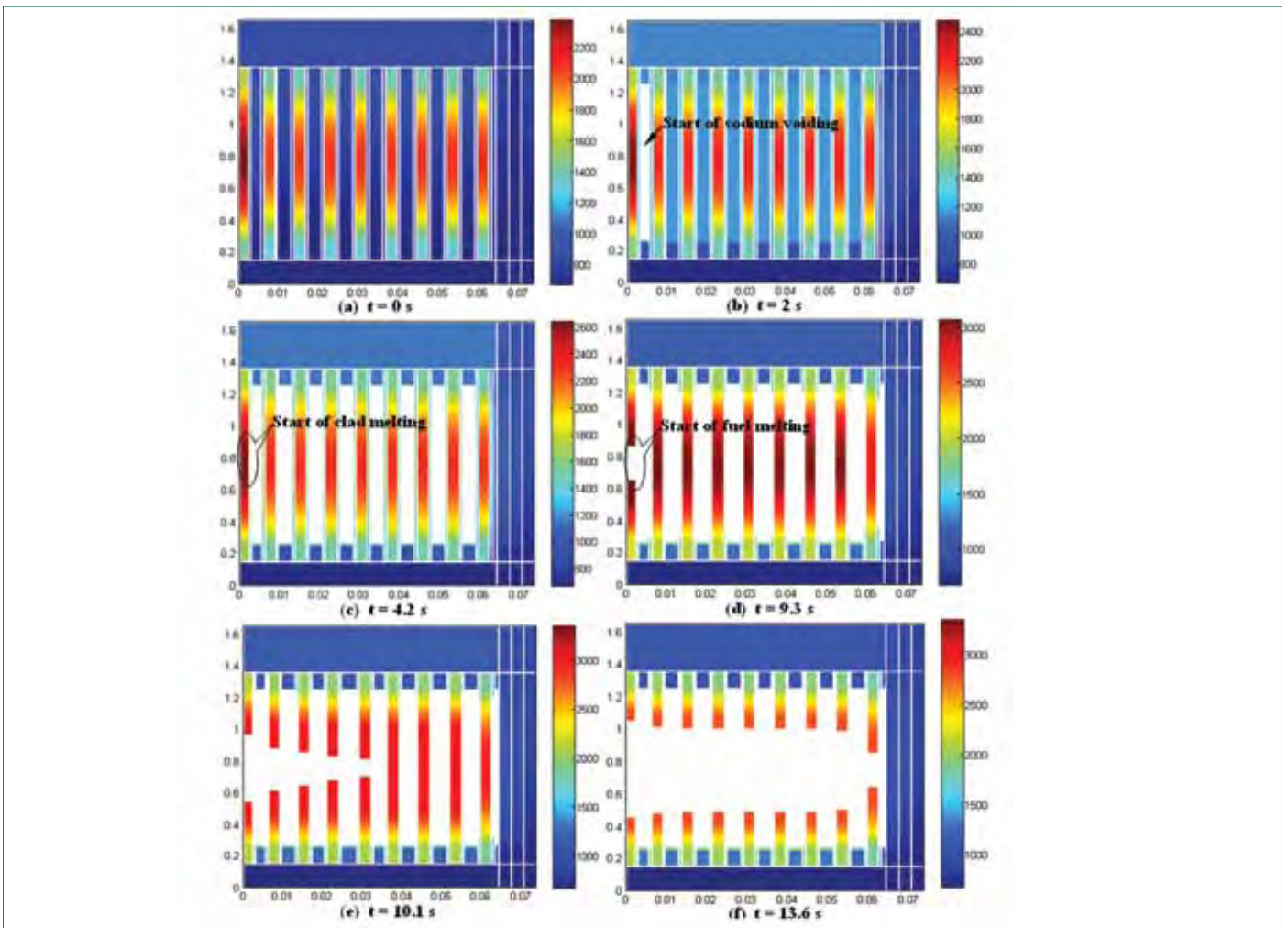

Figure 6: Temperature distribution in blocked SA during Stage-I: (a) Normal operation, (b) Onset of sodium voiding, (c) Onset of clad melting, (d) Onset of fuel melting, (e) Incoherent melting of fuel pins and (f) Onset of fuel melting in peripheral row

of the active zone and forms a steel blockage around still standing fuel pins. Clad melting in the blocked subassembly completes by ~8.5 seconds after start of total instantaneous blockage. The evolution of temperature from sodium void to clad melting and start of fuel break-up can be observed in Figure 6d. Fuel break-up is first noticed in the central pin at ~9.3 seconds and proceeds further to neighboring rows. Peripheral row fuel break-up is observed at about 13.8 seconds after total instantaneous blockage. The fuel melting and the formation of the fuel pool in the blocked subassembly completes in ~17 seconds. The continuous rise in the temperature of fuel, clad and sodium in blocked subassembly results in very small inter-subassembly heat transfer and it is noted that total instantaneous blockage in the subassembly cannot be detected in the Stage-I by monitoring neighboring subassembly thermocouple reading.

Stage-II

The rate of damage progression to hexcan wall at any instant during molten fuel attack depends upon various parameters that influence the heat transfer and material property variation due to phase change during hexcan melting. It was seen that blocked subassembly hexcan melts down completely within 0.8 seconds after molten fuel attack. It is to be noted that the inter-wrapper sodium flow rate is inadequate to prevent hexcan melting. The heat transfer from fuel pool during stage-II over a very short duration (0.8 seconds) is very small resulting in no appreciable rise in the neighboring subassembly thermocouple reading.

Stage-III

The melt front advancing towards the neighboring subassembly after blocked subassembly failure suffers a sufficient heat loss. This results in cooling and solidification of a thin layer of fuel at the melt front before forming a pool surrounded by relatively cold neighboring subassembly hexcan. It shall be highlighted that t = 0 seconds corresponds to molten fuel attack on the neighboring hexcan. It is observed in Figure 7 that the melting speed of hexcan
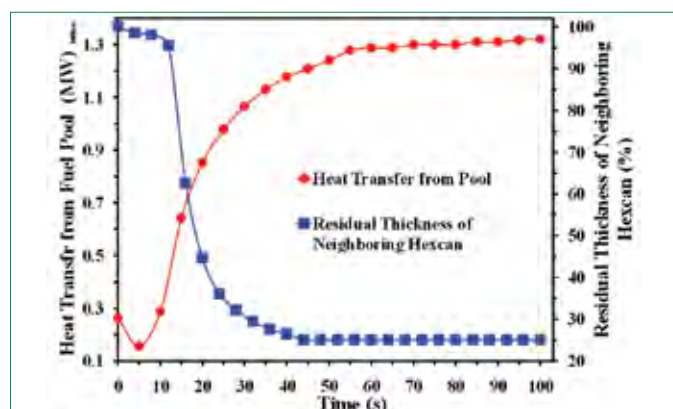

Figure 7: Evolution of instantaneous radial heat transfer rate from the pool to neighboring subassembly hexcan and corresponding residual thickness of the neighboring hexcan during stage-III (t = 0 seconds corresponds to molten fuel attack on the neighboring SA hexcan)

is low at the beginning of fuel-steel contact and it intensifies later. This is due to poor thermal conductivity of the fuel and time delay for natural convection to set-up. Melting speed which is rapid after melting the first hexcan element, decreases later due to enhanced heat absorption by neighboring subassembly sodium consequent to decrease in the residual thickness of hexcan. About 50% of hexcan thickness melts within ~17.5 seconds after molten fuel attack. Hexcan melting nearly ceases when the residual thickness is 25 % at ~42 seconds. On the other hand, heat transfer rate from pool to neighboring hexcan continues to rise even after 42 seconds and stabilizes finally attaining a value of 1.33 MW (which is 1/6th of 8 MW) at about 75 seconds after molten fuel attack.

The temperature rise of neighboring subassembly sodium was rapid till ~3.5 seconds after the molten fuel attack which decreases after ~3.5 seconds due to freezing of fuel. The thermocouple reading due to temperature rise of sodium flowing in the neighboring subassembly during stage-III was calculated considering various values of thermocouple time constant. It was seen that a temperature rise of 10 °C (threshold for reactor SCRAM) is recorded at ~19 seconds after molten fuel attack for a time constant of 8 seconds. The corresponding residual thickness of neighboring hexcan is 53% indicating that the total instantaneous blockage occurrence can be detected during stage-III by monitoring the neighboring subassembly sodium outlet temperature.

Summary

A 2-dimensional transient thermal model based on enthalpy formulation has been developed to predict initiation and propagation of sodium void and clad/fuel melting in a completely blocked fuel subassembly of a SFR. The computational model has been validated against international benchmark results. The model accounts for discrete rows of fuel pins and axial distribution of power. The damage progression is conceived to progress in three stages. During stage-I, no significant inter-subassembly heat transfer takes place inhibiting early detection of this event (before neighboring subassembly is damaged). Eventually, a molten fuel pool is formed which is held by the frozen steel mass at the bottom and hexcan walls of six neighboring subassembly. Vigorous natural convection is observed within the fuel pool that leads to enhanced heat transfer to the neighboring subassembly in stage-III. The transient natural convection within the pool is predicted by solving the 2-dimensonal mass, momentum and energy equations along with turbulence parameters. In this process, the neighboring subassembly hexcan walls partially melt before the reactor trips based on signal from core monitoring thermocouples. Based on detailed parametric studies, it is established that the damage initiated by total instantaneous blockage does not propagate beyond seven subassemblies.

Reported by
L. Ravi and Colleagues
Reactor Design Group

Visit of Dignitaries

Dr. Y.V.N. Krishna Murthy, Distinguished Scientist, ISRO & Director, National Remote Sensing Centre, Hyderabad during the IGC Colloquium

Dr. Y.V.N. Krishna Murthy, Distinguished Scientist, ISRO & Director, National Remote Sensing Centre, Hyderabad delivered IGC Colloquium on the topic "Space Technology and its Applications for National Development" on March 16, 2017

Dr. Knut W. Urban and Dr. Srikumar Banerjee during the IGC Colloquium

Dr. Knut W. Urban, Ernst Ruska Centre for Microscopy and Spectroscopy with Electrons, Juelich, and RWTH Aachen University, Aachen / Germany delivered IGC Colloquium on the topic "Picometer Transmission Electron Microscopy" on March 30, 2017. Dr. Srikumar Banerjee, Homi Bhabha Chair Professor at Bhabha Atomic Research Centre accompanied the guest during his visit

National Science Day
February 28, 2017

Ms. Vinya Sankaran Vasu addressing the audience during National Science Day

The programme commenced with welcome address by Dr. M. Sai Baba, Director, Resources Management Group, followed by inaugural address by Dr. A.K. Bhaduri, Distinguished Scientist and Director, IGCAR. On this occasion, Dr. B. Venkatraman, Director, Health Safety and Environment Group, delivered a lecture on "R&D related to Health and Societal Applications at IGCAR". Ms. Vinya Sankaran Vasu, Deputy Controller of Examinations, National Board for Examination in Rehabilitation and Special Education Consultant, National Institute for Empowerment of Persons with Multiple Disabilities, Muttukad, Tamil Nadu was consented to be the guest of honor and delivered a special address on "Information and Communication Technology and Assistive Technology for Individuals with Disabilities". Shri S.S. Boopathy, AO(P) proposed the vote of thanks.

Collaboration with VSSC, Trivandrum on VIKRAM Processor
February 9, 2017

As part of indigenization of I&C systems for Fast Breeder Reactor, it is proposed to utilize the indigenously developed I&C components and the expertise available in various other Government departments. Towards this, a collaborative development programme with VSSC, Trivandrum has been initiated. Indigenously developed VIKRAM 1601 processor by VSSC, Trivandrum is being received by Director, EIG, IGCAR.

Dr. K. Sivan, Director, VSSC Trivandrum, Shri K. Madhusoodanan, Director, EIG, Ms. T. Jayanthi, Head, RTSD, IGCAR during handing over ceremony of VIKRAM 1601 Processor

Awards and Honours

Dr. M. Sai Baba has been conferred with "Doctor of Science" (Honoris Causa) by Dr. M.G.R. Educational and Research Institute University, Chennai for his outstanding contributions in the fields of Mass Spectrometry, Nuclear Engineering and Training School Programmes

Dr. Sandip Kumar Dhara has been elected as a "Fellow" of The Royal Society of Chemistry and has become a "Member" of American Physical Society

Best Paper/Poster Award

Manufacturing Experiences of Large Stroke Welded Disc Bellows for Nuclear Applications

Shri S.C.S.P Kumar Krovvidi, Shri B.K. Sreedhar, Shri N. Mahendran, Shri G. Padmakumar, Shri S.Raghupathy, Shri Sudhakar Naik ,Shri R. Gopalakrishnan

IEEE sponsored International Conference on Advances in Mechanical, Industrial, Automation and Management Systems (AMIAMS 2017) held in Department of Mechanical Engineering, MNNIT, Allahabad during February 3-5, 2017

Best Paper Award

Exploring the Font Attributes of Microsoft Word: A Steganographic Perspective

Shri R. Bala Krishnan, Shri Prasanth Kumar Thandra, Dr. M. Sai Baba

International Conference on Frontiers in Engineering, Applied Sciences and Technology (FEAST' 17) held at National Institute of Technology, Tiruchirappalli, during March 31 - April 1, 2017

Best Paper Award

Oxygen Potential Analysis of Molybdenum in MOX Fuel

Shri Ronit Kumar Panda, Dr. S. Clement Ravichandar, Dr. M. Sai Baba

13th DAE-BRNS Nuclear and Radiochemistry Symposium (NUCAR-2017) at KIIT University, Bhubaneswar, during February 6-10, 2017

Best Poster Award

Indian pond-heron